



# The Gassmann–Burgers Model to Simulate Seismic Waves at the Earth Crust And Mantle

JOSÉ M. CARCIONE,<sup>1</sup> FLAVIO POLETTO,<sup>1</sup> BIANCAMARIA FARINA,<sup>1</sup> and ARONNE CRAGLIETTO<sup>1</sup>

**Abstract**—The upper part of the crust shows generally brittle behaviour while deeper zones, including the mantle, may present ductile behaviour, depending on the pressure–temperature conditions; moreover, some parts are melted. Seismic waves can be used to detect these conditions on the basis of reflection and transmission events. Basically, from the elastic–plastic point of view the seismic properties (seismic velocity and density) depend on effective pressure and temperature. Confining and pore pressures have opposite effects on these properties, such that very small effective pressures (the presence of overpressured fluids) may substantially decrease the P- and S-wave velocities, mainly the latter, by opening of cracks and weakening of grain contacts. Similarly, high temperatures induce the same effect by partial melting. To model these effects, we consider a poro-viscoelastic model based on Gassmann equations and Burgers mechanical model to represent the properties of the rock frame and describe ductility in which deformation takes place by shear plastic flow. The Burgers elements allow us to model the effects of seismic attenuation, velocity dispersion and steady-state creep flow, respectively. The stiffness components of the brittle and ductile media depend on stress and temperature through the shear viscosity, which is obtained by the Arrhenius equation and the octahedral stress criterion. Effective pressure effects are taken into account in the dry-rock moduli using exponential functions whose parameters are obtained by fitting experimental data as a function of confining pressure. Since fluid effects are important, the density and bulk modulus of the saturating fluids (water and steam) are modeled using the equations provided by the NIST website, including supercritical behaviour. The theory allows us to obtain the phase velocity and quality factor as a function of depth and geological pressure and temperature as well as time frequency. We then obtain the PS and SH equations of motion recast in the velocity–stress formulation, including memory variables to avoid the computation of time convolutions. The equations correspond to isotropic anelastic and inhomogeneous media and are solved by a direct grid method based on the Runge–Kutta time stepping technique and the Fourier pseudospectral method. The algorithm is tested with success against known analytical solutions for different shear viscosities. An example shows how anomalous conditions of pressure and temperature can in principle be detected with seismic waves.

**Key words:** Brittle, ductile, Burgers model, Gassmann theory, seismic-wave simulation, attenuation, Fourier method.

## 1. Introduction

The seismic characterization of the brittle and ductile parts of the crust and mantle is essential in earthquake seismology and geothermal exploration, since it plays an important role in determining the nucleation depth of earthquakes (Meissner and Strehlau 1982) and the availability of geothermal energy (Manzella et al. 1998). Carcione and Poletto (2013) introduced an elastic–plastic rheology to model ductile behaviour on the basis of variations of the shear modulus as a function of temperature. The ductile medium mainly flows when subject to deviatoric stress, while it does not show major flow under hydrostatic stress, such that the deformation is mainly associated with the shear modulus of the medium. The criterion by which the shear modulus is affected is based on the octahedral stress, a scalar quantity that is invariant under coordinate transformations. The flow viscosity is a function of temperature and confining pressure, determined by the geothermal gradient and the tectonic stresses. Carcione and Poletto (2013) have also modeled the effects of anisotropy and seismic attenuation, based on the Burgers model (see Fig. 1) (the Maxwell and Zener model are particular cases of this model) [see Mainardi and Spada (2011)]. The Zener part of the model is used to model the viscoelastic motion with no plastic flow, obtained as the limit of infinite plastic viscosity. Seismic losses are solely due to shear deformations.

Carcione et al. (2014) implement the previous model to simulate wave propagation in isotropic and anelastic inhomogeneous media and compute

<sup>1</sup> Istituto Nazionale di Oceanografia e di Geofisica Sperimentale (OGS), Borgo Grotta Gigante 42c, Sgonico, 34010 Trieste, Italy. E-mail: jcarcione@inogs.it

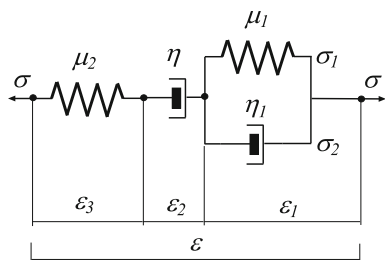


Figure 1

Mechanical representation of the Burgers viscoelastic model for shear deformations (e.g. Carcione 2015).  $\sigma$ ,  $\epsilon$ ,  $\mu$  and  $\eta$  represent stress, strain, shear modulus and viscosity, respectively, where  $\eta_1$  describes seismic relaxation while  $\eta$  is related to plastic flow and processes such as dislocation creep

synthetic seismograms. They obtain the PS and SH equations of motion recast in the velocity–stress formulation, including memory variables to avoid the computation of time convolutions. The equations are based on a generalization of the Lamé constants to the viscoelastic case. The equations are solved by a direct grid method based on the Runge–Kutta time stepping technique and the Fourier pseudospectral method. A realistic example illustrates the computation of surface and reverse-VSP synthetic seismograms in the presence of an abrupt brittle–ductile transition.

The poroelastic case has been studied by Jaya et al. (2010), who performed laboratory measurements and used Gassmann equation as a predictive model, which assumes that the grain and dry-rock moduli are independent of temperature. Hence, their model is restricted to a range of temperatures where melting does not occur, contrary to the model developed by Carcione and Poletto (2013). Jaya et al. (2010) show that P-wave velocity decreases with increasing temperature and that at higher temperatures bubbles and thermal microfractures occur. The measurements also show that at low temperatures seismic attenuation decreases with temperature due to the rapid decrease in the fluid viscosity, and that at high temperatures the attenuation increases because of the generation of bubbles and microfractures. The presence of bubbles is required to fit the velocities at a pore pressure of 80 bar and high temperatures (150 to 250 °C), using the Wood model to obtain the effective fluid bulk modulus. On the other hand, the

quality factor of the P wave varies from 300 at 125 °C to 25 at 250 °C at a frequency of 400 kHz, explained by the authors due to a decrease in fluid viscosity of one order of magnitude.

In this work, we extend the theory and modeling algorithm to the poro-viscoelasticity case to model explicitly the effects of the saturating fluids, generally water and steam at different pressure–temperature conditions, including supercritical behaviour. Moreover, the new theory allows us to model the effects of the confining and pore pressures on the stiffness moduli of the medium. Pressure effects are introduced using an effective stress law of exponential form (e.g. Kaselow and Shapiro 2004; Carcione 2015), by which at constant effective pressure the acoustic (and transport) properties of the rock remain constant. The effective pressure depends on the difference between the confining and pore pressures.

Seismic waves are useful to study the structure of the Earth on the basis of forward modeling, inversion and interpretation (Poletto and Miranda 2004). To this purpose, proper computational-geophysics techniques are essential (e.g. Carcione et al. 2002, 2010). In this work, we simulate seismic wave propagation in heterogeneous media using a direct grid method (a full-wave solver). The differential equations are solved in the time domain using memory variables (Carcione 2015) and generalising the bulk and shear moduli, other than the Lamé constants as in Carcione et al. (2014). This new approach is more physical since those moduli are the fundamental deformations of the medium. We assume isotropic media and plane strain conditions and obtain the differential equations of motion for 2-D PS and SH waves. The equations are recast in the velocity–stress formulation and solved with the Runge–Kutta and the Fourier methods, regarding the time and spatial discretizations (e.g. Carcione 2015).

## 2. Mean and Octahedral Stresses

We use the octahedral-stress theory to describe the deformation of the ductile layer. In Cartesian coordinates  $(x, y, z)$ , we define the octahedral stress as:

$$\sigma_o = \frac{1}{3} \sqrt{(\sigma_v - \sigma_h)^2 + (\sigma_v - \sigma_H)^2 + (\sigma_h - \sigma_H)^2}, \quad (1)$$

where the  $\sigma$ 's are the stress components in the principal system, corresponding to the vertical ( $v$ ) lithostatic stress, and the maximum ( $H$ ) and minimum ( $h$ ) horizontal tectonic stresses (see Fig. 2a). Figure 2b shows the octahedral stress as a function of the octahedral strain. When the stress vector associated with the normal to the octahedral plane is generated, its components in the principal directions are the eigenstresses (or principal stresses). Alternatively, it has two components—one normal to the plane (which has a magnitude equal to the mean stress) and one tangential to the plane which has a

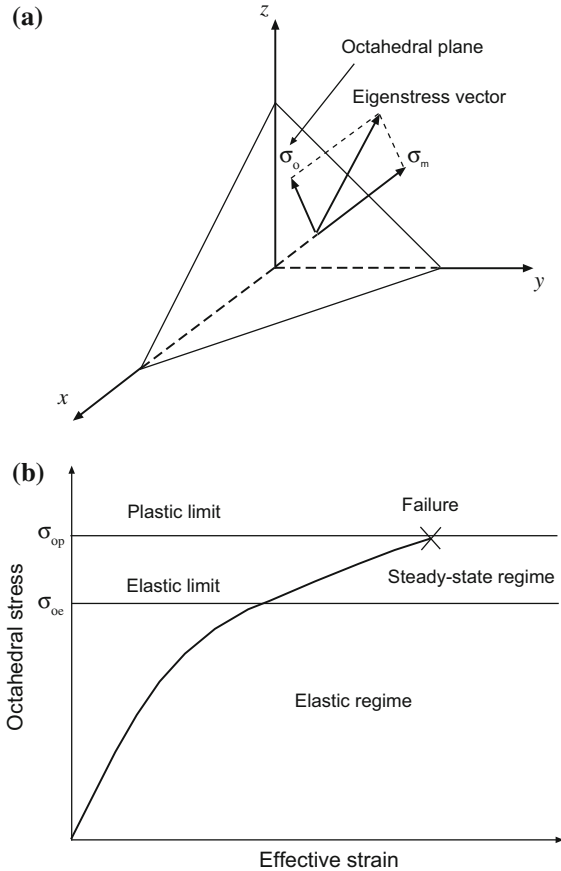


Figure 2

Mean and octahedral stresses (a) versus octahedral (effective) strain (b). The octahedral-stress vector, which is a measure of the shear deformation, lies on the octahedral plane. The normal to this surface makes the same angle with the direction of the three principal stresses  $\sigma_v$ ,  $\sigma_h$  and  $\sigma_H$

magnitude equal to the octahedral stress (the latter is proportional to the magnitude of the deviatoric stress).

The rock starts to yield when  $\sigma_o$  exceeds the elastic octahedral-stress limit  $\sigma_{oe}$ . Below this limit, there is gradual creep deformation when constant stress is applied. Then, if  $\sigma_o$  is lower than the elastic limit  $\sigma_{oe}$ , the material follows a viscoelastic stress–strain relation. If  $\sigma_o$  lies between  $\sigma_{oe}$  and the plastic limit  $\sigma_{op}$ , steady-state flow occurs. Beyond  $\sigma_{op}$  failure is likely to occur.

### 3. The Gassmann–Burgers Mechanical Model

The constitutive equation, including both the viscoelastic and ductile behaviour, can be written as a generalization of stress–strain relation reported in Carcione and Poletto (2013) to the poroelastic case. The Burgers model is a series connection of a dashpot and a Zener model as can be seen in Fig. 1. The usual expression in the time domain is the creep function

$$\chi = \left( \frac{t}{\eta} + \frac{1}{\mu_0} \left[ 1 - \left( 1 - \frac{\tau_\sigma}{\tau_\epsilon} \right) \exp(-t/\tau_\epsilon) \right] \right) H(t) \quad (2)$$

(Carcione et al. 2006; Carcione 2015), where  $t$  is time and  $H(t)$  is the Heaviside function. The quantities  $\tau_\sigma$  and  $\tau_\epsilon$  are seismic relaxation times,  $\mu_0$  is the relaxed shear modulus (see below) and  $\eta$  is the flow viscosity describing the ductile behaviour related to shear deformations. The frequency-domain shear modulus  $\mu$  can be obtained as  $\mu_B = [\mathcal{F}(\dot{\chi})]^{-1}$ , where  $\mathcal{F}$  denotes time Fourier transform and a dot above a variable denotes time derivative. It gives

$$\mu_B = \frac{\mu_0(1 + i\omega\tau_\epsilon)}{1 + i\omega\tau_\sigma - \frac{i\mu_0}{\omega\eta}(1 + i\omega\tau_\epsilon)}, \quad (3)$$

where  $i = \sqrt{-1}$  and  $\omega$  is the angular frequency. The relaxation times can be expressed as:

$$\tau_\epsilon = \frac{\tau_0}{Q_0} \left( \sqrt{Q_0^2 + 1} + 1 \right), \quad \tau_\sigma = \tau_\epsilon - \frac{2\tau_0}{Q_0}, \quad (4)$$

where  $\tau_0$  is a relaxation time such that  $\omega_0 = 1/\tau_0$  is the center frequency of the relaxation peak and  $Q_0$  is the minimum quality factor.

The limit  $\eta \rightarrow \infty$  in Eq. (3) recovers the Zener kernel to describe the behaviour of the brittle material, while  $\tau_\sigma \rightarrow 0$  and  $\tau_\epsilon \rightarrow 0$  yield the Maxwell model used by Dragoni (1990) and Dragoni and Pondrelli (1991):

$$\mu_B = \mu_0 \left( 1 - \frac{i\mu_0}{\omega\eta} \right)^{-1} \quad (5)$$

(e.g. Carcione 2015). For  $\eta \rightarrow 0$ ,  $\mu_B \rightarrow 0$  and the medium becomes a fluid. Moreover, if  $\omega \rightarrow \infty$ ,  $\mu_B \rightarrow \mu_0\tau_\epsilon/\tau_\sigma$ , and  $\mu_0$  is the relaxed ( $\omega = 0$ ) shear modulus of the Zener element ( $\eta = \infty$ ).

The viscosity  $\eta$  can be expressed by the Arrhenius equation (e.g. Carcione et al. 2006; Montesi 2007). It is related to the steady-state creep rate  $\dot{\epsilon}$  by

$$\eta = \frac{\sigma_o}{2\dot{\epsilon}}, \quad (6)$$

where  $\sigma_o$  is the octahedral stress. The strain rate can be expressed as:

$$\dot{\epsilon} = A\sigma_o^n \exp(-E/RT) \quad (7)$$

(e.g. Gangi 1981, 1983; Carcione et al. 2006; Carcione and Poletto 2013), where  $A$  and  $n$  are constants,  $E$  is the activation energy,  $R = 8.3144 \text{ J/mol}^\circ\text{K}$  is the gas constant and  $T$  is the absolute temperature. The form of the empirical relation (7) is determined by performing experiments at different strain rates, temperatures and/or stresses (e.g. Gangi 1983; Carter and Hansen 1983).

To obtain the equation of motion to describe wave propagation in poroelastic media, we express the dry-rock bulk moduli as:

$$K_m = K_0 g_1(p_e), \quad \text{and} \quad \mu_m = \mu_B g_2(p_e), \quad (8)$$

where  $g_r(p_e)$ ,  $r = 1, 2$  defines the dependence of the moduli on the effective pressure  $p_e = p_c - np$ , where  $p_c$  is the confining pressure,  $p$  is the pore (fluid) pressure,  $n$  is the effective stress coefficient, and  $K_0$  and  $\mu_0$  are the bulk and shear moduli at infinite effective pressure and  $\eta = \infty$  (or  $\omega = \infty$ ).

Laboratory experiments show that under hydrostatic pore pressure, confining stress and differential pressure dependences of elastic moduli are phenomenologically described by the following relationship:

$$g_r(p_e) = a_r + b_r p_e - c_r \exp(-p_e/p_r^*), \quad r = 1, 2 \quad (9)$$

(Kaselow and Shapiro 2004; Carcione 2015), where  $a_r$ ,  $b_r$ ,  $c_r$  and  $p_r^*$  are fitting parameters for a given set of measurements. If  $n_r = 1$ ,  $p_e = p_d = p_c - p$ , the differential pressure.

The simplest form of function  $g$ , in good agreement with experimental data, is obtained for  $a_r = 1$ ,  $b_r = 0$ ,  $c_r = 1 - d_r$  and  $n_r = 1$ , i. e.,

$$g_r(p_d) = 1 - (1 - d_r) \exp(-p_d/p_r^*), \quad r = 1, 2, \quad (10)$$

where  $g_r = 1$  for  $p_d \rightarrow \infty$  (e.g. very high confining pressure) and  $g_r = d_r$  for  $p_d \rightarrow 0$  (pore pressure equal to the confining pressure).

The wet-rock Gassmann–Burgers poroelasticity bulk and shear moduli are given by

$$K = K_m + \alpha^2 M \quad \text{and} \quad \mu(\omega) = \mu_m(\omega) \quad (11)$$

and

$$\alpha = 1 - \frac{K_m}{K_s} \quad \text{and} \quad M = \frac{K_s}{1 - \phi - K_m/K_s + \phi K_s/K_f}, \quad (12)$$

where  $\phi$  is the rock porosity and  $K_s$  and  $K_f$  are the solid and fluid bulk moduli, respectively (e.g. Carcione 2015). In particular,  $K_f$  depends on pressure and temperature.

The bulk density is

$$\rho = (1 - \phi)\rho_s + \phi\rho_f, \quad (13)$$

where  $\rho_s$  and  $\rho_f$  are the grain and fluid densities, respectively.

#### 4. Equations of Motion

To obtain the equations of motion to describe wave propagation, it is convenient to consider the Burgers relaxation function

$$\psi(t) = [A_1 \exp(-t/\tau_1) - A_2 \exp(-t/\tau_2)]H(t), \quad (14)$$

(Carcione 2015; Carcione and Poletto 2013), where we have redefined  $\mu_0$  such that the pressure dependence has been incorporated, for simplicity, into this stiffness, i.e.

$$\begin{aligned} \mu_0 &\rightarrow \mu_0 g_2(p_d), \\ \tau_{1,2} &= -\frac{1}{\omega_{1,2}} \quad \text{and} \quad A_{1,2} = \frac{\mu_1 \mu_2 + \omega_{1,2} \eta_1 \mu_2}{\eta_1 (\omega_1 - \omega_2)}. \end{aligned} \quad (15)$$

and

$$\begin{aligned} (2\eta_1 \omega_{1,2}) &= -b \pm \sqrt{b^2 - 4\mu_1 \mu_2 \eta_1}, \\ b &= (\mu_1 + \mu_2) \eta + \mu_2 \eta_1. \end{aligned} \quad (16)$$

In terms of the relaxation times and  $\mu_0$ , it is

$$\mu_1 = \frac{\mu_0 \tau_\epsilon}{\tau_\epsilon - \tau_\sigma}, \quad \mu_2 = \mu_0 \frac{\tau_\epsilon}{\tau_\sigma}, \quad \eta_1 = \mu_1 \tau_\epsilon. \quad (17)$$

The complex shear modulus is

$$\mu = \mathcal{F}(\dot{\psi}) = i\omega \left( \frac{A_1 \tau_1}{1 + i\omega \tau_1} - \frac{A_2 \tau_2}{1 + i\omega \tau_2} \right). \quad (18)$$

It can be verified that Eqs. (3) and (18) coincide.

#### 4.1. 2D Propagation of PS waves

The stress–strain relation is given by

$$\sigma_{ij} = K \vartheta \delta_{ij} + 2\psi * \left( \dot{\epsilon}_{ij} - \frac{1}{3} \dot{\epsilon}_{kk} \delta_{ij} \right), \quad (19)$$

where  $\sigma$  are stress components,  $\epsilon$  are strain components,  $\vartheta = \epsilon_{ii}$  is the dilatation,  $\partial_i$  indicates a spatial derivative with respect to the variable  $x_i$ ,  $i = 1, 2, 3$  ( $x_1 = x$ ,  $x_2 = y$  and  $x_3 = z$ ),  $\delta$  is Kronecker delta and “\*” denotes time convolution.

The velocity–stress formulation requires

$$\dot{\sigma}_{ij} = K \partial_k v_k \delta_{ij} + \dot{\psi} * \left( \partial_i v_j + \partial_j v_i - \frac{2}{3} \partial_k v_k \delta_{ij} \right), \quad (20)$$

where  $v$  are particle-velocity components and we have used the displacement–strain relations (e.g. Carcione 2015).

All the convolutions have the form  $\dot{\psi} * \partial_i v_j$  and can be avoided by introducing memory variables. We obtain

$$\dot{\psi} * \partial_i v_j = A_1 (\partial_i v_j + e_{ij}^{(1)}) - A_2 (\partial_i v_j + e_{ij}^{(2)}), \quad i, j = 1, 3, \quad (21)$$

where

$$e_{ij}^{(l)} = \varphi_l H * \partial_i v_j, \quad \varphi_l = -\frac{1}{\tau_l} \exp(-t/\tau_l), \quad l = 1, 2, \quad (22)$$

which satisfy

$$\dot{e}_{ij}^{(l)} = -\frac{1}{\tau_l} (\partial_i v_j + e_{ij}^{(l)}). \quad (23)$$

#### 4.2. Propagation of PS Waves

Let us consider plane-strain conditions with propagation in the  $(x, z)$ -plane. The stress–strain relation (20) becomes

$$\begin{aligned} \dot{\sigma}_{xx} &= K (\partial_x v_x + \partial_z v_z) + \frac{2}{3} \dot{\psi} * (2\partial_x v_x - \partial_z v_z), \\ \dot{\sigma}_{zz} &= K (\partial_x v_x + \partial_z v_z) + \frac{2}{3} \dot{\psi} * (2\partial_z v_z - \partial_x v_x), \\ \dot{\sigma}_{xz} &= \dot{\psi} * (\partial_x v_z + \partial_z v_x) \end{aligned} \quad (24)$$

Substituting the memory variables according to Eq. (21), we obtain

$$\begin{aligned} 3\dot{\sigma}_{xx} &= [3K + 4(A_1 - A_2)] \partial_x v_x + [3K - 2(A_1 - A_2)] \partial_z v_z \\ &\quad + 2(2A_1 e_{xx}^{(1)} - 2A_2 e_{xx}^{(2)} - A_1 e_{zz}^{(1)} + A_2 e_{zz}^{(2)}), \\ 3\dot{\sigma}_{zz} &= [3K + 4(A_1 - A_2)] \partial_z v_z + [3K - 2(A_1 - A_2)] \partial_x v_x \\ &\quad + 2(2A_1 e_{zz}^{(1)} - 2A_2 e_{zz}^{(2)} - A_1 e_{xx}^{(1)} + A_2 e_{xx}^{(2)}), \\ \dot{\sigma}_{xz} &= (A_1 - A_2) (\partial_x v_z + \partial_z v_x) + A_1 (e_{xz}^{(1)} + e_{zx}^{(1)}) \\ &\quad - A_2 (e_{xz}^{(2)} + e_{zx}^{(2)}). \end{aligned} \quad (25)$$

On the other hand, the dynamical equations of motion are

$$\begin{aligned} \dot{v}_x &= \frac{1}{\rho} (\partial_x \sigma_{xx} + \partial_z \sigma_{xz}) + s_x, \\ \dot{v}_z &= \frac{1}{\rho} (\partial_x \sigma_{xz} + \partial_z \sigma_{zz}) + s_z \end{aligned} \quad (26)$$

(e.g. Carcione 2015), where  $s_i$  are source components.

The equations of motion are given by Eqs. (23), (25) and (26) in the unknown vector  $\mathbf{v} = (v_x, v_z, \sigma_{xx}, \sigma_{zz}, \sigma_{xz}, e_{ij}^{(l)})^\top$ . In matrix notation

$$\dot{\mathbf{v}} = \mathbf{M} \cdot \mathbf{v} + \mathbf{s}, \quad (27)$$

where  $\mathbf{M}$  is a  $13 \times 13$  matrix containing the material properties and spatial derivatives.

### 4.3. Propagation of SH Waves

The stress–strain relations describing pure shear motion in the  $(x, z)$ -plane are

$$\dot{\sigma}_{xy} = \dot{\psi} * \partial_x v_y \quad \text{and} \quad \dot{\sigma}_{zy} = \dot{\psi} * \partial_z v_y. \quad (28)$$

Applying the same procedure as in the PS case, we obtain

$$\begin{aligned} \dot{\sigma}_{xy} &= (A_1 - A_2)\partial_x v_y + A_1 e_{xy}^{(1)} - A_2 e_{xy}^{(2)}, \\ \dot{\sigma}_{zy} &= (A_1 - A_2)\partial_z v_y + A_1 e_{zy}^{(1)} - A_2 e_{zy}^{(2)}, \end{aligned} \quad (29)$$

with

$$\begin{aligned} \dot{e}_{xy}^{(l)} &= -\frac{1}{\tau_l} (\partial_x v_y + e_{xy}^{(l)}), \\ \dot{e}_{zy}^{(l)} &= -\frac{1}{\tau_l} (\partial_z v_y + e_{zy}^{(l)}), \quad l = 1, 2. \end{aligned} \quad (30)$$

The dynamical equation of motion is

$$\dot{v}_y = \frac{1}{\rho} (\partial_x \sigma_{xy} + \partial_z \sigma_{zy}) + s, \quad (31)$$

where  $s$  is the source (e.g. Carcione 2015).

The equations of motion are given by equations (29), (30) and (31) in the unknown vector  $\boldsymbol{\sigma} = (v_y, \sigma_{xy}, \sigma_{zy}, e_{xy}^{(1)}, e_{xy}^{(2)})^\top$  and can be recast as Eq. (27) with matrix  $\mathbf{M}$  of dimension  $7 \times 7$ . It can be shown that  $A_1 = \mu$  and  $A_2 = 0$  yields the lossless case.

This particle-velocity/stress formulation differs from that given in Carcione et al. (2014); since in the present work, the bulk and shear moduli are assumed as basic elasticity constants, instead of the Lamé constants, to introduce the memory variables.

### 4.4. Wave Velocities and Attenuation

The wave velocities can be obtained from the density and Eq. (19), which represent the stress–strain relations of an isotropic-viscoelastic medium, where the bulk modulus ( $K$ ) and shear relaxation function ( $\psi$ ) can be identified. We make use of the frequency-domain version of the stress–strain relations and  $\mu = [\mathcal{F}(\dot{\psi})]$ . Note that  $\dot{\psi} * \dot{\chi} = \delta$ , where  $\delta$  is Dirac's function (e.g. Carcione 2015). Then, from Eq. (11), the complex and frequency-dependent P- and S-wave velocities are

$$v_P(\omega) = \sqrt{\frac{K + 4\mu(\omega)/3}{\rho}}, \quad \text{and} \quad v_S(\omega) = \sqrt{\frac{\mu(\omega)}{\rho}}, \quad (32)$$

respectively, where the density is given by Eq. (13).

For homogeneous waves in isotropic media, the phase velocity and attenuation factors are given by

$$c = \left[ \text{Re} \left( \frac{1}{v} \right) \right]^{-1} \quad (33)$$

and

$$\alpha = -\omega \text{Im} \left( \frac{1}{v} \right), \quad (34)$$

and the P- and S-wave quality factors are given by

$$Q = \frac{\text{Re}(v^2)}{\text{Im}(v^2)} \quad (35)$$

(e.g. Carcione 2015), where  $v$  represent either  $v_P$  or  $v_S$ .

## 5. Examples

We consider sample KTB 61C9b (amphibolite) reported in Popp and Kern (1994) (their Table II and Fig. 3). Dry- and wet-rock velocities values are given in Table 1, where the measurements were performed at room temperature. Closure of cracks with confining pressure is reflected in the values of the compliant porosity given in Table II of Popp and Kern (1994), ranging from 0.28% at 12 MPa to 0.01% at 200 MPa. The stiff porosity  $\phi$  is not reported in Popp and Kern (1994) but can be obtained by fitting the P-wave wet-rock ultrasonic velocities. Since the experiments of Popp and Kern (1994) were performed at 2 MHz, the low-frequency Gassmann Eq. (11) is not valid. At high frequencies, the squirt flow mechanism is dominant implying a stiffening of the rock (e.g. Carcione and Gurevich 2011).

The dry-rock moduli at low frequencies are

$$K_m = (1 - \phi)\rho_s \left( v_P^2 - \frac{4}{3}v_S^2 \right), \quad \mu_m = (1 - \phi)\rho_s v_S^2, \quad (36)$$

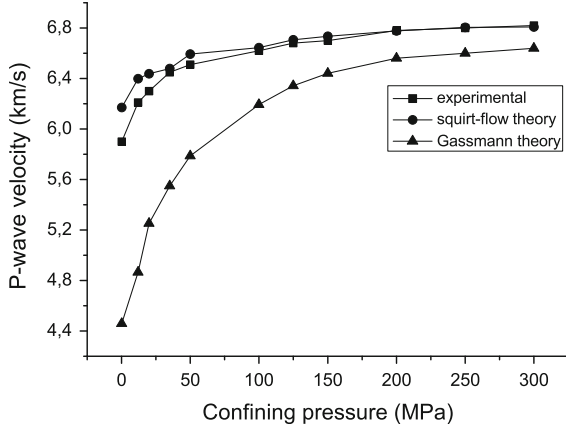


Figure 3  
Experimental and theoretical wet-rock P-wave velocities as a function of confining pressure

Table 1

Wave velocities versus confining pressure

Pressure (MPa)	$v_P$ (dry) (km/s)	$v_S$ (dry) (km/s)	$v_P$ (wet) (km/s)	$v_S$ (wet) (km/s)
0.1	4.50	2.82	5.90	3
12	4.91	3.13	6.21	3.35
20	5.30	3.25	6.30	3.45
35	5.60	3.35	6.45	3.55
50	5.84	3.45	6.51	3.60
100	6.25	3.65	6.62	3.70
125	6.40	3.75	6.68	3.75
150	6.50	3.80	6.70	3.78
200	6.62	3.86	6.78	3.82
250	6.66	3.90	6.80	3.85
300	6.70	3.91	6.82	3.86
350	6.75	3.92	–	–
400	6.80	3.93	–	–
450	6.82	3.93	–	–
500	6.85	3.94	–	–
550	6.88	3.95	–	–
600	6.90	3.95	–	–

where  $v_P$  and  $v_S$  are the velocities of the dry rock. Substituting Eqs. (36) into (32), the wet-rock Gassmann velocities are

$$v_P = \sqrt{\frac{K + 4\mu_m/3}{\rho}} \quad v_S = \sqrt{\frac{\mu_m}{\rho}}. \quad (37)$$

On the other hand, using the squirt-flow theory to obtain the velocities at high frequencies, the dry-rock moduli  $K_m$  and  $\mu_m$  are replaced by

$$\frac{1}{K'_m} = \frac{1}{K_h} + \left[ \left( \frac{1}{K_m} - \frac{1}{K_h} \right)^{-1} + \left( \frac{1}{K'_f} - \frac{1}{K_s} \right)^{-1} \phi_c^{-1} \right]^{-1},$$

$$\frac{1}{\mu'_m} = \frac{1}{\mu_m} - \frac{4}{15} \left( \frac{1}{K_m} - \frac{1}{K'_m} \right), \quad (38)$$

in equation (11), where  $K_m$  and  $\mu_m$  are the dry-rock bulk and shear moduli given by Eq. (36),  $K_h$  is the dry-rock bulk modulus at a confining pressure where all the compliant pores are closed, i.e. an hypothetical rock without the soft porosity, and  $\phi_c$  is the compliant porosity (see Carcione and Gurevich 2011). The key quantity in Eq. (38) is the effective bulk modulus of the fluid saturating the soft pores:

$$K_f^* = i\omega\eta^*, \quad (39)$$

where  $\omega$  is the angular frequency,

$$\eta^* = \frac{3}{2} \left( \frac{R}{h} \right)^2 \eta_f, \quad (40)$$

is an effective viscosity,  $\eta_f$  is the fluid viscosity,  $R$  is the radius of the crack and  $h$  is its thickness, such that  $h/R$  is the aspect ratio of the cracks (see Carcione and Gurevich 2011).

We consider  $\rho_s = 3 \text{ g/cm}^3$  (Schön 2011),  $\rho_f = 1.04 \text{ g/cm}^3$ ,  $K_s = 133.45 \text{ GPa}$  (this value is deduced from Table II of Popp and Kern (1994), intrinsic velocity data at 200 MPa),  $K_f = 2.34 \text{ GPa}$ ,  $\eta_f = 0.001 \text{ Pa s}$ ,  $h/R = 0.003$  (see Fig. 7 in Popp and Kern (1994)),  $K_h = 0.5K_s$  and a frequency of 2 MHz. The crack porosity  $\phi_c$  follows the trend given in that Table II as a function of the confining pressure (see above). Since the new P-wave velocity,  $v$ , is complex, we compute the phase velocity in the usual way as  $1/\text{Re}(1/v)$ , where “Re” takes real part (e.g. Carcione 2015). The fit of the wet-rock velocity yields a stiff porosity  $\phi = 5\%$ . Figure 3 shows the fit and the low-frequency (seismic) Gassmann velocity.

Having the stiff porosity, we obtain the dry-rock bulk and shear moduli at seismic frequencies from Eqs. (8) and (10) using Eq. (36),

$$g_1 = 1 - (1 - 0.39) \exp(-p_d/65),$$

$$g_2 = 1 - (1 - 0.52) \exp(-p_d/62), \quad (41)$$

where  $K_0 = 69.84 \text{ GPa}$ ,  $\mu_0 = 43.57 \text{ GPa}$  and  $p_d$  is given in MPa. This fit corresponds to  $\eta = \infty$ , i.e.

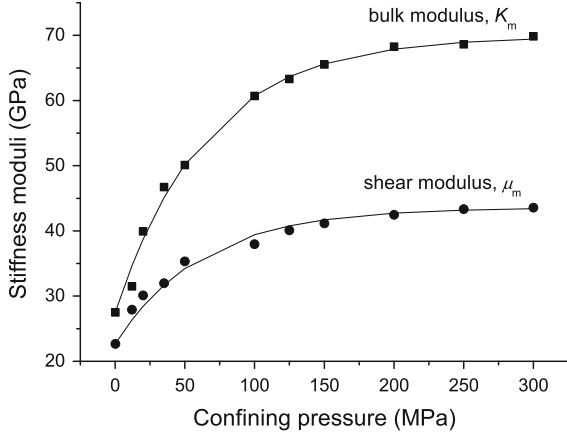


Figure 4

Fit of the dry-rock bulk and shear moduli as a function of confining pressure

$\mu_B = \mu_0$ . Figure 4 shows the fit of the stiffness moduli.

Next, we obtain the wave velocities and quality factors at different temperature–pressure conditions. The shear seismic loss parameter is obtained from empirical equations derived by Castro et al. (2008) for the crust in Southern Italy. They report  $Q_0 = 18.8 f^{1.7}$  for the upper crust and up to a frequency of 10 Hz. In the examples, we consider a frequency of  $f = 3$  Hz, with  $\omega_0 = 2 \pi f$ , which gives  $Q_0 = 122$ . The temperature is a function of depth through the geothermal gradient  $G$  as  $T = zG$ , where  $z$  is depth and  $G = 60$  °C/km in our calculations. The lithostatic stress is  $\sigma_v = -\bar{\rho}gz = -p_c$ , where  $\bar{\rho} = 2400$  kg/m<sup>3</sup> is the average density and  $g = 9.81$  m/s<sup>2</sup> is the gravity constant. To obtain the octahedral stress (1), we consider a simple model based on the gravity contribution at depth  $z$ . The horizontal stresses can be estimated as:

$$\sigma_H = \frac{\nu\sigma_v}{1 - \nu}, \quad \text{and} \quad \sigma_h = \xi\sigma_H \quad (42)$$

where

$$\nu = \frac{3K_0 - 2\mu_0}{2(3K_0 + \mu_0)} \quad (43)$$

is the Poisson ratio. The factor  $\nu/(1 - \nu)$  lies between 0.25 and 1 for  $\nu$  ranging from 0.2 to 0.5, with the latter value corresponding to a liquid (hydrostatic stress). The parameter  $\xi \leq 1$  has been introduced to model additional effects due to tectonic activity

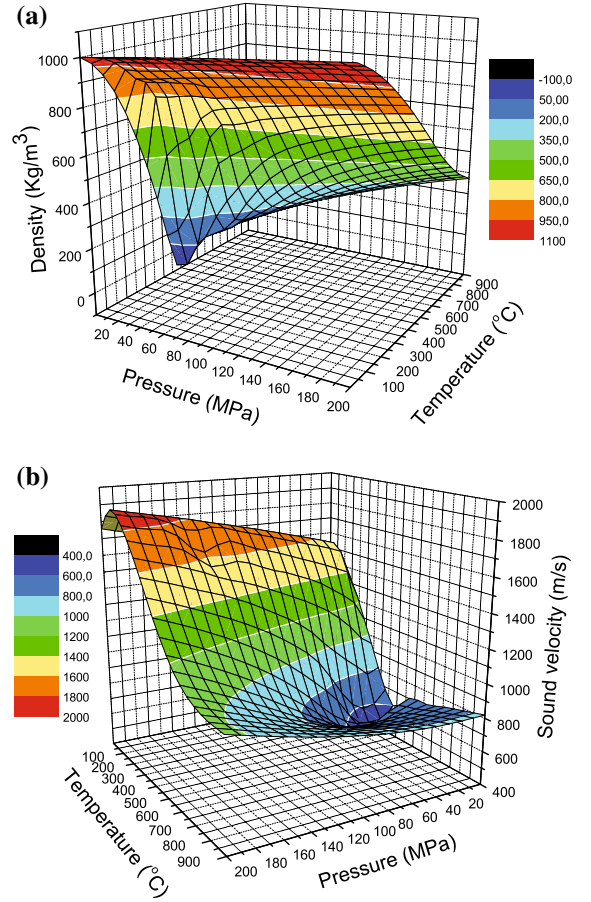


Figure 5

Water density (a) and sound velocity (b) for a wide range of pressures and temperatures (data taken from the NIST website)

(anisotropic tectonic stress). Furthermore, we consider  $A_\infty = 100$  (MPa)<sup>-n</sup> s<sup>-1</sup>,  $E = 134$  kJ/mol and  $n = 2$ , and take  $\xi = 0.8$ . The above degree of stress anisotropy is consistent with values at prospective depths provided by Hegret (1987) for the Canadian Shield, and in agreement with data reported in Engelder (1993, p. 91).

The water properties as a function of pressure and temperature are obtained from the fluid thermo-physical database provided in the website of the National Institute of Standards and Technology (NIST), collected from laboratory measurements by Lemmon et al. (2005). In “Thermophysical Properties of Fluid Systems”, we choose water (1) and Isothermal Properties (3). The range of allowable values is [0, 1000] °C and [0, 1000] MPa. To analyse the seismic properties in the presence of overpressure

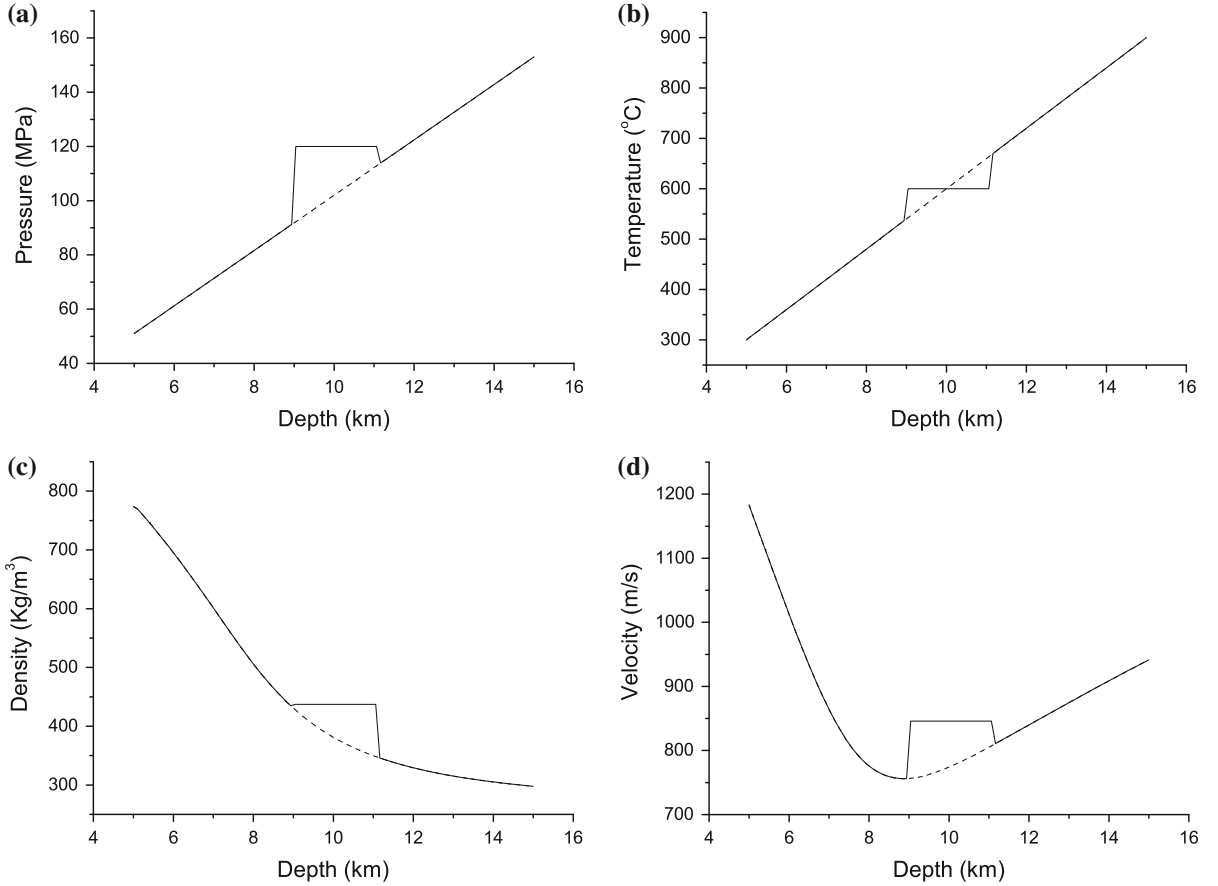


Figure 6

Pore pressure (a), temperature (b), water density (c) and water velocity (d) as a function of depth, according to the NIST website. The *dashed* and *solid* lines correspond to normal and anomalous conditions. A layer between 9 and 11 km has high p-T conditions

and anomalous temperatures, we extract the water density,  $\rho_w$  and sound velocity,  $c_w$ , from the NIST website for the range  $[0, 900]$  °C and  $[0, 200]$  MPa. A 3D plot is shown in Fig. 5. The blue zone in the density surface corresponds to the vapor phase. The bulk modulus is then given by  $K_f = \rho_w c_w^2$ .

A state of hydrostatic pore pressure is given by  $p = \bar{\rho}_f g z$ , where  $\bar{\rho}_f = 1000 \text{ kg/m}^3$  is an average fluid density. We consider a depth range  $[5, 15]$  km, where pore pressure and temperature vary from 50 to 150 MPa and 300 to 900 °C, respectively (the geothermal gradient is 60 °C/km). The experimental density and sound velocity of water are shown in Fig. 6, together with the pressure and temperature profiles, where we consider a high p-T layer between 9 and 11 km (solid lines). Compare these values to the ones at ambient conditions, defined by a temperature of 20 °C and a

pressure of 0.1 MPa: a water density of 998 kg/m<sup>3</sup> and a sound velocity of 1482 m/s. Figure 7 shows the seismic (phase) velocity (a) and quality factor (b) as a function of depth, where the solid and dashed lines correspond to the normal and anomalous cases, respectively. As can be seen, the P-wave velocities decrease after a given viscosity dictated by a critical (transition) temperature (ca. 900 K) and the Arrhenius equation. The P-wave attenuation has a maximum at this transition and at higher temperatures the medium becomes an anisotropic fluid whose quality factors are solely determined by the dilatational losses. Indeed, the lack of the shear losses increases the quality factor and the material behaves fluid like with weaker attenuation. This is consistent with the fact that a pure solid and a pure liquid have weak attenuation and partial saturation (melting in

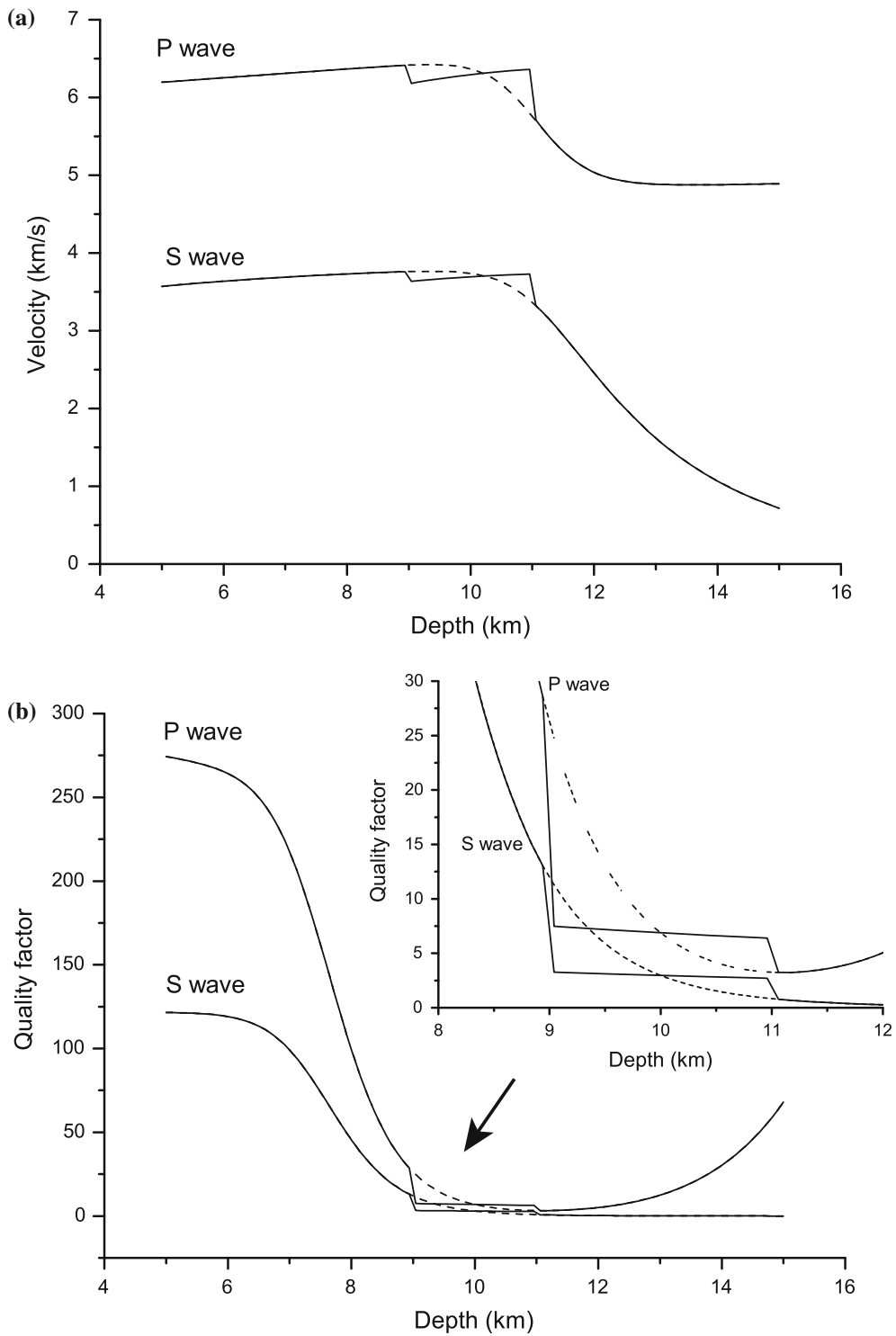


Figure 7

Seismic velocities (a) and quality factors (b) as a function of depth. The dashed and solid lines correspond to normal and anomalous conditions. A layer between 9 and 11 km has high p-T conditions

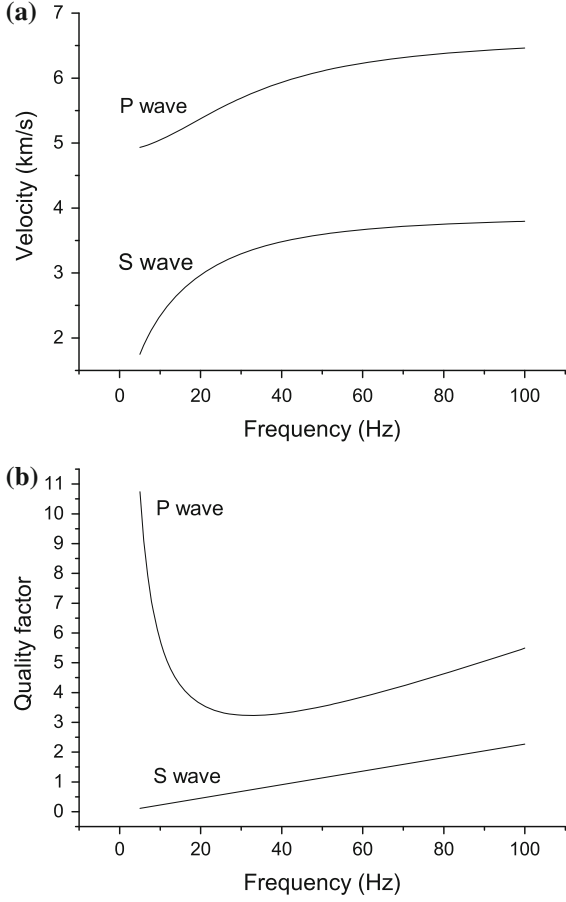


Figure 8

Phase velocity (a) and quality factor (b) as a function of frequency for a temperature of 803 °C

this case) shows lower  $Q$  factors, similar to the behaviour of the mesoscopic-loss mechanism (e.g. Singh et al. 2000; Carcione 2015). By this mechanism, wave energy is converted to diffusion energy of the Biot slow-mode type, when the heterogeneities of the medium are smaller than the seismic wavelength but greater than a characteristic pore scale.

Figure 8 shows the behaviour of the phase velocity and quality factor as a function of frequency for a temperature of 803 °C and normal pore pressure conditions, according to Fig. 7 (in this case  $\eta = 1.6 \times 10^8$  Pa s). At this temperature, the S wave behaves diffusively, as shown in the next example, and the P wave is very dispersive due to the low  $Q$  factor. Beyond a given temperature, the algorithm becomes unstable due to diffusive character of the S wave, since the system of equations becomes hyperbolic (P

wave)-parabolic (S wave) and a suitable solver should be implemented for this situation. Something similar occurs with Biot's equations of poroelasticity, where the slow P wave is diffusive at seismic frequency. Appropriate solvers are outlined in Carcione (2015).

We simulate wave propagation with a full-wave numerical algorithm based on the Fourier pseudo-spectral method. First, we test the numerical code against an analytical solution for PS waves in homogeneous media (see Carcione et al. 2014 for the expression of the solution). To compute the transient responses, we use a Ricker wavelet of the form:

$$h(t) = \left(u - \frac{1}{2}\right) \exp(-u), \quad u = \left[\frac{\pi(t - t_s)}{P}\right]^2, \quad (44)$$

where  $P$  is the period of the wave (the distance between the side peaks is  $\sqrt{6}P/\pi$ ) and we take  $t_s = 1.4P$ . Its frequency spectrum is

$$H(\omega) = \left(\frac{P}{\sqrt{\pi}}\right) \bar{u} \exp(-\bar{u} - i\omega t_s), \quad \bar{u} = \left(\frac{\omega}{\omega_p}\right)^2, \quad \omega_p = \frac{2\pi}{P}. \quad (45)$$

The peak frequency is  $f_p = 1/t_p$ .

We consider the conditions at two depths to test the algorithm, namely 5 and 13 km. In the second case, the S wave disappears. The seismic quality factor is  $Q_0 = 40$  and  $\omega_0 = 2\pi f_p$ . The numerical mesh has  $231 \times 231$  grid points and a grid spacing of 30 m. The source is a vertical force with  $f_p = 10$  Hz and the receiver is located at  $x = z = 1.2$  km from the source. The solution is computed using a time step of 1 ms. Figure 9 shows the comparison between the numerical and analytical PS-wave solutions for  $\eta = 2.3 \times 10^{14}$  Pa s (a, b) and  $\eta = 2.1 \times 10^8$  Pa s (c, d), where (a) and (c) correspond to  $v_x$  and (b) and (d) to  $v_z$ . As can be seen, the agreement is excellent.

Second, we consider homogeneous media with three set of properties, namely, those at 8 km depth, 11 km depth (bottom of the high p-T layer) and 13 km depth, where the conditions are normal. We assume  $Q_0 = 122$  at  $f_0 = 3$  Hz. In the second case, the pore pressure is hydrostatic ( $p = 78$  MPa),

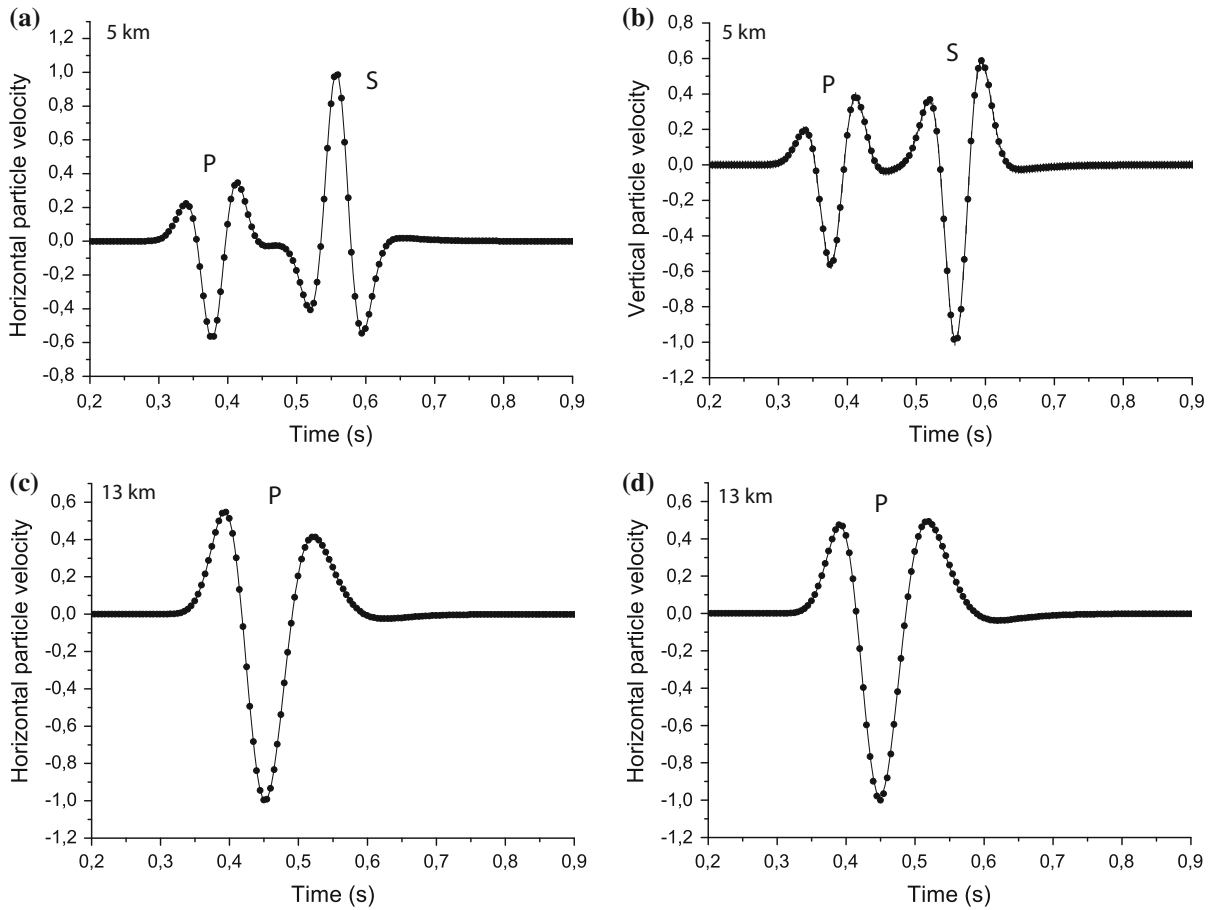


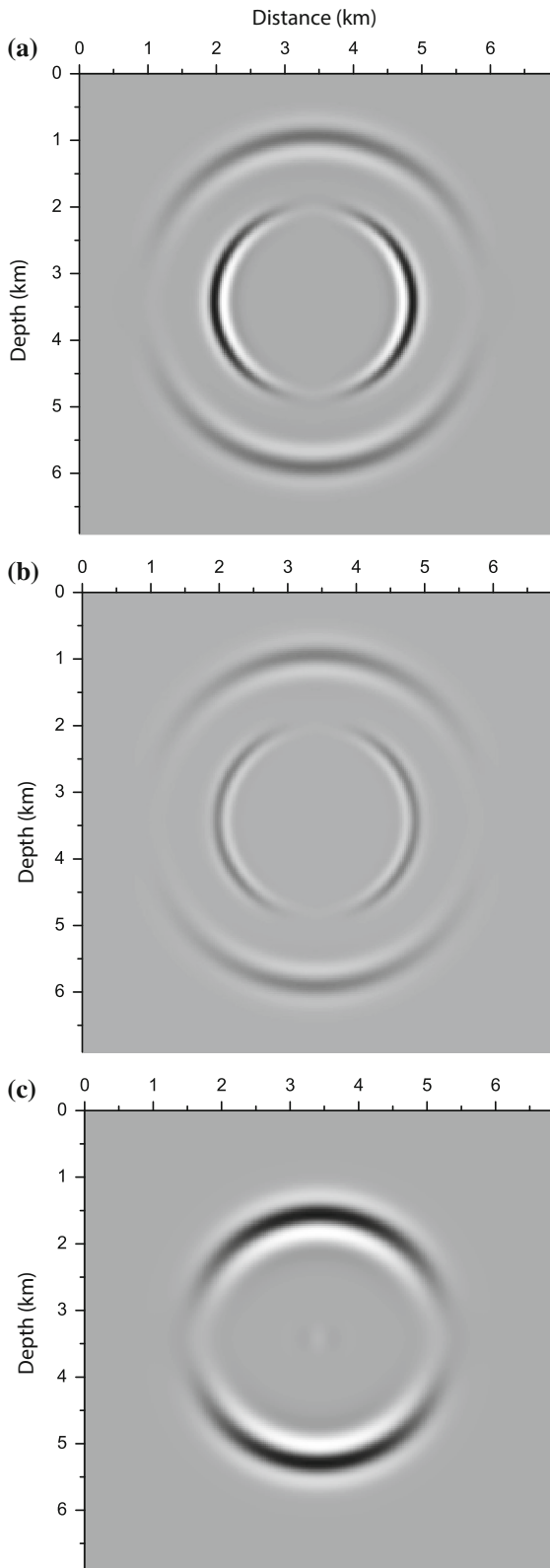
Figure 9

Comparison between the analytical (*solid line*) and numerical (*symbols*) PS-wave solutions. The fields are normalized. The amplitude in **c**, **d** is much lower than in **a** and **b** due to the attenuation caused by the plastic viscosity

$p_c = 188$  MPa and  $T = 482$  °C. We use the same mesh and source time history of the previous simulation and a vertical force. Absorbing boundaries of size 50 grid points are implemented at the sides of the mesh. The algorithm uses a time step of 1 ms to propagate the wavefield 500 steps. Figure 10 shows three snapshots, corresponding to 8 km (a), 11 km (b) and 13 km (c) depths, where the P and S waves can be observed in (a) and (b), while it has disappeared in (c) due to the very low quality factor (see Fig. 7b). The snapshot in (c) has been re-scaled with respect to (a) and (b), since attenuation is stronger. The amplitude is higher at 8 km, where the  $Q$ -factor for P waves is 97 against 7 at 11 km. This is because the temperature is lower and the viscosity is higher. A much lower viscosity has damped the S wave in (c).

Moreover, the P wavefront is smaller, since the P-wave phase velocity is lower at 13 km (see Fig. 7a).

Finally, we compute a cross-well seismogram, corresponding to two vertical wells separated by a distance of 600 m. This example is an ideal experiment since the wells are very deep, but it is useful to illustrate the propagation characteristics in very hot magmatic poro-viscoelastic rocks. Similar configurations could be considered to study wavefields in a reciprocal sense, i.e. as in seismic while drilling applications (Aleotti et al. 1999; Poletto and Miranda 2004), interchanging source and receiver, with source in a deep well and receiver in a shallower one (Poletto et al. 2011). A vertical source is located at 8 km depth, 1 km above a layer with the characteristics



◀Figure 10

Snapshots at 0.5 s, corresponding to properties at 8 km (a), 11 km (b) and 13 km (c) depths. The snapshot in (c) has been re-scaled to view the P wavefront

shown in Fig. 7, i.e. the layer is horizontal with the upper interface at 9 km depth and the lower interface at 11 km depth. The signal is recorded at a set of 100 receivers, where the first upper receiver is located at the same depth of the source. The properties and numerical parameters of the simulation are the same used to compute the snapshots in Fig. 10. The seismogram is displayed in Fig. 11. P and S direct waves can be observed and reflected waves (R) at the top and bottom of the layer (relative depths of 1 and 3 km, respectively). The amplitude in the smaller panels has been enhanced by a factor 100. The signal amplitude and phase of the direct events are affected by the presence of anomalous conditions at each depth and this is the main indicator, while the reflected waves are much weaker than the direct waves.

The rheological equation presented here can be further generalized to include explicitly the squirt-flow model (Mavko and Nur 1975; Carcione and Gurevich 2011), and the fractional Burgers model (Mainardi and Spada 2011), which have the potential of better characterizing the time dependence of the relaxation processes involved in wave propagation.

### 6. Conclusions

The Earth crust behaves brittle and ductile depending on the in situ temperature and pressure conditions. We present a methodology to model the seismic properties of the crust, including melting, using a poro-viscoelastic description, based on the Burgers and Gassmann models. In this way, we can model variations of the properties not only due to changes in temperature but also due to confining and pore pressure changes, through the dry-rock stiffness moduli. Moreover, since the theory is based on the Gassmann bulk modulus, variations of the wet-rock seismic velocities can explicitly be computed as a function of the water bulk modulus, with water at normal, critical and supercritical conditions.

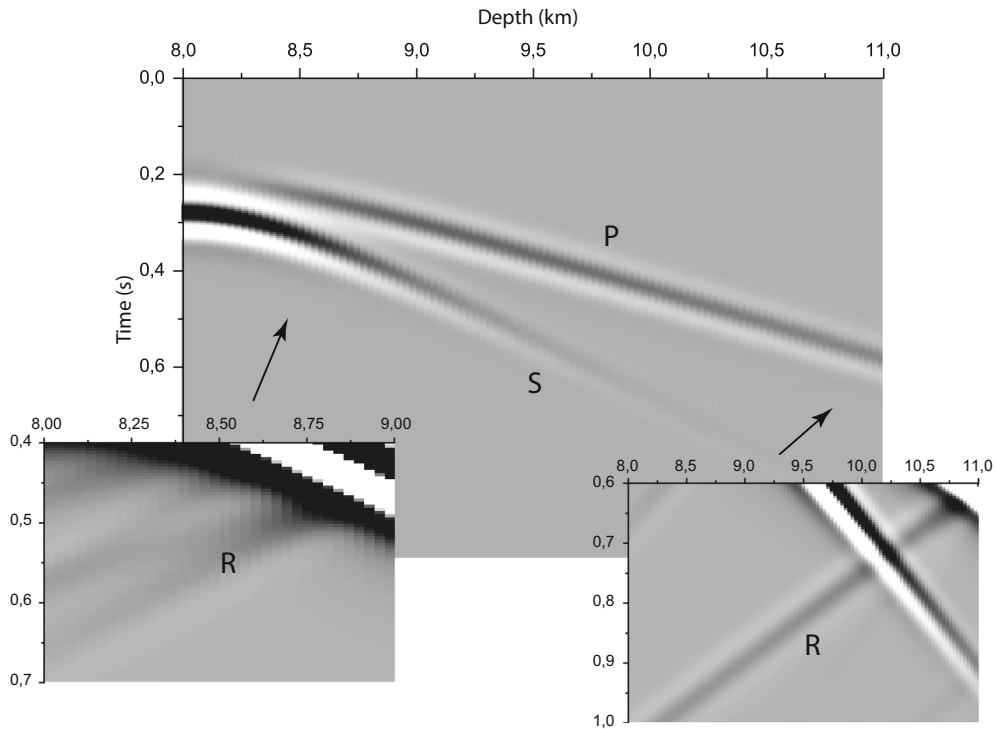


Figure 11

Cross-well seismogram, corresponding to two vertical wells separated by 600 m, going through a layer with the characteristics shown in Fig. 7. The source is located in the left well at 1 km above the layer, and 100 receivers are vertically placed at 600 m offset from the source location (right well). The upper receiver has the same depth of the source. The P and S direct waves can be observed as well as reflected waves (R) at the top and bottom of the layer (depths of 9 and 11 km, respectively). The amplitude in the smaller panels has been enhanced by a factor 100 to view the reflected wave fields

Implementing the stress–strain relation into the equations of momentum conservation yields the wave equation and the phase velocities and quality factors as a function of depth, temperature, pressure and frequency.

We then solve the full-wave equations for P and S waves numerically to obtain synthetic seismograms. The time convolutions appearing in the stress–strain relations are circumvented by introducing memory variables, and the numerical algorithm is based on the Fourier pseudospectral method to compute the spatial derivatives. The modeling technique is successfully tested against known analytical solutions. The methodology applies to any situation where there is melting and to geothermal fields, where water is present at supercritical conditions. The examples illustrate how to compute seismic signals in heterogeneous media, under different conditions of pore pressure, temperature and source frequency.

## REFERENCES

- Aleotti, L., Poletto, F., Miranda, F., Corubolo, P., Abramo, F., & Craglietto, A. (1999). Seismic while-drilling technology: use and analysis of the drill-bit seismic source in a cross-hole survey. *Geophysical Prospecting*, *47*, 25–39.
- Carcione, J. M., 2015. *Wave fields in real media: Wave propagation in anisotropic, anelastic, porous and electromagnetic media*. Handbook of Geophysical Exploration, vol. 38, Elsevier (3rd edition, revised and extended).
- Carcione, J. M., & Gurevich, B. (2011). Differential form and numerical implementation of Biot's poroelasticity equations with squirt dissipation. *Geophysics*, *76*, N55–N64.
- Carcione, J. M., Helle, H. B., & Gangi, A. F. (2006). Theory of borehole stability when drilling through salt formations. *Geophysics*, *71*, F31–F47.
- Carcione, J. M., Herman, G., & ten Kroode, F. P. E. (2002). Seismic modeling. *Geophysics*, *67*, 1304–1325.
- Carcione, J. M., Morency, C., & Santos, J. E. (2010). Computational poroelasticity—a review. *Geophysics*, *75*, A229–A243.
- Carcione, J. M., & Poletto, F. (2013). Seismic rheological model and reflection coefficients of the brittle-ductile transition. *Pure and Applied Geophysics*, doi:10.1007/s00024-013-0643-4.

- Carcione, J. M., Poletto, F., Farina, B., & Craglietto, A. (2014). Simulation of seismic waves at the Earth's crust (brittle-ductile transition) based on the Burgers model. *Solid Earth Discuss*, 6, 1371–1400.
- Carter, N. L., & Hansen, F. D. (1983). Creep of rocksalt. *Tectonophysics*, 92, 275–333.
- Castro, R. R., Gallipoli, M. R., & Mucciarelli, M. (2008). Crustal Q in southern Italy determined from regional earthquakes. *Tectonophysics*, 457(2), 96–101.
- Dragoni, M. (1990). Stress relaxation at the lower dislocation edge of great shallow earthquakes. *Tectonophysics*, 179, 113–119.
- Dragoni, M., & Pondrelli, S. (1991). Depth of the brittle-ductile transition in a transcurent boundary zone. *Pure and Applied Geophysics*, 135, 447–461.
- Engelder, T., 1993. *Stress regimes in the lithosphere*, Princeton University Press.
- Gangi, A. F., 1981. A constitutive equation for one-dimensional transient and steady-state flow of solids. *Mechanical Behavior of Crustal Rocks*, Geophysical Monograph 24, AGU, 275–285.
- Gangi, A. F. (1983). Transient and steady-state deformation of synthetic rocksalt. *Tectonophysics*, 91, 137–156.
- Hegret, G. (1987). Stress assumption for underground excavation in the Canadian Shield. *International Journal of Rock Mechanics and Mining Sciences and Geomechanics Abstracts*, 24, 95–97.
- Jaya, M. S., Shapiro, S. A., Kristinsdóttir, L. H., Bruhn, D., Milsch, H., & Spangenberg, E. (2010). Temperature dependence of seismic properties in geothermal rocks at reservoir conditions. *Geothermics*, 39, 115–123.
- Kaselow, A., & Shapiro, S. A. (2004). Stress sensitivity of elastic moduli and electrical resistivity in porous rocks. *Journal of Geophysics and Engineering*, 1, 1–11.
- Lemmon, E. W., McLinden, M. O., Friend, D. G., 2005. Thermophysical properties of fluid systems. In: Lindstrom, P.J., Mallard, W.G. (eds.), NIST Chemistry Webbook 69, NIST Standard Reference Database, Gaithersburg, MD, USA, <http://webbook.nist.gov/chemistry/>.
- Mainardi, F., & Spada, G. (2011). Creep, relaxation and viscosity properties for basic fractional models in rheology. *The European Physical Journal, Special Topics*, 193, 133–160.
- Manzella, A., Ruggieri, G., Gianelli, G., & Puxeddu, M. (1998). Plutonic-geothermal systems of southern Tuscany: a review of the crustal models. *Mem. Soc. Geol. It.*, 52, 283–294.
- Mavko, G., & Nur, A. (1975). Melt squirt in the asthenosphere. *Journal of Geophysical Research*, 80, 1444–1448.
- Meissner, R., & Strehlau, J. (1982). Limits of stresses in continental crusts and their relation to the depth-frequency distribution of shallow earthquakes. *Tectonics*, 1, 73–89.
- Montesi, L. G. J. (2007). A constitutive model for layer development in shear zones near the brittle-ductile transition. *Geophysical Research Letters*, 34, L08307. doi:10.1029/2007GL029250.
- Poletto, F., Corubolo, P., Schleifer, A., Farina, B., Pollard, J., & Grozdanich, B. (2011). Seismic while drilling for geophysical exploration in a geothermal well. *Transactions, Geothermal Resources Council*, 35(2), 1737–1741.
- Poletto, F., & Miranda, F. (2004). *Seismic while drilling*. Pergamon, Amsterdam: Fundamentals of drill-bit seismic for exploration.
- Popp, T., & Kern, H. (1994). The influence of dry and water saturated cracks on seismic velocities of crustal rocks—a comparison of experimental data with theoretical model. *Surveys in Geophysics*, 15, 443–465.
- Schön, J. H., 2011. *Physical properties of rocks: A workbook*, Handbook of Petroleum Exploration and Production, vol. 8.
- Singh, S. C., Taylor, M. A. J., and Montagner, J. P., 2000. On the presence of liquid in Earth's inner core, *Science* 287, March Issue.

(Received May 9, 2016, revised November 18, 2016, accepted November 22, 2016)